N_{Fo} = Fourier number = $\alpha t/D^2$
N_{Gr} = Grashof number = $\dfrac{g\, D^3|\beta_\infty(T_w - T_\infty)|}{\nu^2}$
N_{Nu} = average Nusselt number
$N_{Nu_{ex}}$ = experimental Nusselt number = $\bar{h}L/k$
N_{Pr} = Prandtl number = $\mu C_p/k$
N_{Ra} = Rayleigh number = $N_{Gr}N_{Pr}$
N_{Sh} = Sherwood number
Q = total heat transfer to sphere, cal.
t = time, sec.
t_1 = initial time, time of first reliable reading, sec.
t_2 = final time, last reading taken, sec.
T = temperature, °C.
T_f = mean film temperature = $(T_w + T_\infty)/2$, °C.
T_w = wall temperature, °C.
T_∞ = bulk fluid temperature, °C.
V_0, V_1 = volume of ice sphere at times t_0 and t_1, cc.
V_L = volume of lead sinker, cc.
w, W = apparent weight, g.
W_L = weight of lead sinker, cc.

Greek Letters

α = thermal diffusivity, sq. cm./sec.
β_∞ = coefficient of expansion defined in *(12, 15)*, $(°C.)^{-1}$
γ = density ratio, ρ_l/ρ_s
ΔC = concentration difference, g./cc.
ΔH_f = latent heat of fusion $(H_l - H_s)$, cal./g.
ϵ = fractional change in radius or diameter = $(D_0 - D_1)/D_0$
μ = viscosity, poise
ν = kinematic viscosity, sq. cm./sec.
ρ = density, g./cc.
ρ_g = gas density, g/cc.
Φ = degree of melting function, defined by (12)

Subscripts

° = evaluated a 0°C., also referring to time t_0
∞ = evaluated far from the wall
l = liquid
s = solid
w = evaluated at the wall
1, 2 = calculated at times t_1, t_2

LITERATURE CITED

1. Bird, R. B., W. E. Stewart, and E. L. Lightfoot, "Transport Phenomena," p. 248, Wiley, New York (1965).
2. "Chementator," *Chem. Eng.*, 74, 20 (1967).
3. Chiang, T., A. Ossin, and C. L. Tien, *J. Heat Transfer*, 86C, 4 (1964).
4. Dumore, J. M., H. J. Merk, and J. A. Prins, *Nature*, **172**, 460 (1953).
5. Ede, A. J., *Appl. Sci. Res.*, **A5**, 458 (1955).
6. Koh, J. C. Y., and J. F. Price, *J. Heat Transfer*, **87C**, 2 (1965).
7. Kranse, A. A., and A. J. Schenk, *Appl. Sci. Res.*, **A15**, 397 (1966). Schenk, A. J., and F. A. M. Schenkels, *Appl., Sci. Res.*, **19**, 465 (1968).
8. Merk, H. J., *ibid.*, **A4**, 435 (1954).
9. ———, and J. A. Prins, *ibid.*, 11, 195, 207.
10. Powell, R. W., *Advan. Phys.*, **7**, 276 (1958).
11. "Review of the Properties of Snow and Ice," SIPRE Rept. 4, p. 88, (July, 1951).
12. Schechter, R. S., and H. S. Isbin, *AIChE J.*, **4**, No. 1, 81 (1958); Schechter, R. S., Ph.D. thesis, Univ. Minn., Minneapolis (1956).
13. Tkachev, A. G., *AEC-Tr-3405*, translated from a Publication of the State Power Press, Moscow-Leningrad (1953).
14. Van der Burgh, S., *Appl. Sci. Res.*, **A9**, 293 (1960).
15. Vanier, C. R., and Chi Tien, *Chem. Eng. Progr. Symposium Ser. No. 82*, **64**, 240 (1968).
16. ———, M. S. thesis, Syracuse Univ., N. Y. (1967).
17. ———, and Chi Tien, *Chem. Eng. Sci.*, **22**, 1747 1967).

Manuscript received March 28, 1968; revision received July 23, 1968; paper accepted July 26, 1968.

Mass Transfer in a Nonuniform Impinging Jet

M. T. SCHOLTZ
Toronto Coppersmithing Company Limited, Scarborough, Ontario
and OLEV TRASS
University of Toronto, Toronto, Ontario

Part I. Stagnation Flow-Velocity and Pressure Distribution

A theoretical solution for the impingement flow of a jet with a parabolic velocity distribution is given. Viscous generation and diffusion of vorticity in the jet were neglected. Experimental velocity and pressure distributions measured in an impinging jet of air originating with Poiseuille flow compare well with theory, thus justifying the assumption of inviscid flow. Pressure distributions on the deflecting surface were independent of nozzle height in the range 1 to 12 nozzle radii. For lower nozzle heights the effect of the constriction of flow between the nozzle and the surface followed the predicted behavior.

Impinging jets of fluid are frequently used in industry for heating and cooling operations. In the aero space sciences, special efforts have been made to interpret the behavior of axisymmetric impinging jets with application to vertical take off and landing devices. In applications where heat or mass transfer is of importance, interest in impinging jets is directed to phenomena associated with the region of the viscous boundary layer which develops on the impingement surface.

Figure 1 is a sketch of an axisymmetric impinging jet. The flow in the oncoming jet may be laminar or turbulent; the time average flow may be uniform (left-hand side) or nonuniform (right-hand side), (Figure 1). An example of the turbulent nonuniform flow would be an impinging, fully developed, free jet.

Several theoretical and experimental studies have been made of the flow and heat or mass transfer using impinging jets. The theoretical analyses (*1* to *6*) have usually been restricted to the uniform impinging jet. The applicability of such solutions is limited to cases where the nozzle-to-plate distance is less than five nozzle diameters. For larger nozzle distances, a free jet profile develops and the impinging jet is nonuniform.

Correlation between the published experimental heat and mass transfer data of independent workers is not good in terms of controlled variables. Experimental conditions such as turbulence level, form of the impinging jet velocity profile, and surface conditions probably vary considerably between different workers; the effects of these variables are not well known for impinging jets.

Gardon and Akfirat (*7*) have shown that the turbulence level in the impinging jet is an important variable in transfer processes near the stagnation point. Sutera, Maeder, and Kestin (*8*) have shown theoretically that due to rapid stretching of radially aligned vortex filaments in the neighborhood of the stagnation point, turbulence amplification can take place with a resulting enhancement of heat transfer.

With dissolution mass transfer from a solid surface, surface erosion and roughness effects are important (*9*, *10*). Ranz and Dickson (*3*) have studied simultaneous heat and mass transfer with high rates of mass transfer; interface mobility of the liquid pool used in their study was examined. Drying in the stagnation region of an impinging, turbulent jet has been studied by Schrader (*11*); the effect of surface roughness was evaluated. Schrader also determined the main features of the impinging jet from experimental velocity measurements.

The subject of this paper is the nonuniform, turbulence-free, impinging jet. The stagnation of a jet formed by fully developed laminar pipe flow has been examined. Such a jet, free of turbulence, is easily simulated in the laboratory and the mass transfer at the stagnation region due to the nonuniform jet alone can be evaluated.

For convenience this paper is divided into two sections. Part I is a theoretical and experimental examination of fluid flow of the laminar nonuniform jet. On the assumption that inviscid rotational flow pertains, velocity profiles and pressure distributions are calculated and compared with experimental measurements.

Part II deals with theoretical calculations and experimental measurements of mass transfer from the flat impingement surface to the stagnating jet. A generalized exact boundary layer solution for nonsimilar axisymmetric flow is matched with the results of Part I, permitting the calculation of mass transfer coefficients for comparison with experiment.

EQUATIONS GOVERNING THE MOTION

In the absence of body forces the Navier-Stokes equation for constant properties are:

$$\frac{D\vec{V}}{Dt} = \frac{\partial \vec{V}}{\partial t} + (\vec{V} \cdot \nabla) \cdot \vec{V} = \frac{1}{\rho}\,\mathrm{grad}\,p + \nu \nabla^2 \vec{V} \quad (1)$$

Two further equations can be written, the continuity equation,

$$\nabla \cdot \vec{V} = 0 \quad (2)$$

and an expression defining the vorticity,

$$\nabla \times \vec{V} = \vec{\zeta} \quad (3)$$

Taking the curl of (1) and using (2) and (3) gives,

$$\nabla \times (\vec{V} \times \vec{\zeta}) = -\nu \nabla \times (\nabla^2 \vec{V}) \quad (4)$$

Evaluating Equation (4) for Poiseuille flow gives the result,

$$\nabla \times (\vec{V} \times \vec{\zeta}) = 0 \quad (5)$$

Hence, in fully developed laminar pipe flow, the viscous generation and diffusion of vorticity have reached a steady state and viscosity plays no role in maintaining the velocity distribution. The terms on the left-hand side of Equation (4) represent convection of vorticity and nonviscous vorticity generation by the bending and stretching of vortex filaments. The terms on the right-hand side take account of the viscous generation and diffusion of vorticity.

In the case of the present jet, excluding for the moment the viscous boundary layer regions, vorticity in the impingement region is of the order of U_N/R. In the regions of the viscous boundary layers, namely along the deflecting surface and near the edge of the jet, vorticity is of the high order of U_N/δ.

It may be expected that where vorticity is of low order, convection and nonviscous generation of vorticity would mainly describe the flow and the viscous terms of Equation (4) could be neglected. Such an assumption is not valid in the boundary layer regions containing high order vorticity; in these regions Prandtl's boundary layer equations may be applied.

For present theoretical purposes, flow in the nonuniform impinging jet will be divided into two regions:

1. rotational, inviscid flow in the body of the impinging jet

$$\nabla \times (\vec{V} \times \vec{\zeta}) = 0 \quad (6)$$

considered in Part I, and

2. viscous boundary layer flow near the impingement surface

$$\nabla \cdot \vec{V} + \frac{1}{\rho}\,\mathrm{grad}\,p = \nu \nabla^2 \vec{V} \quad (7)$$

considered in Part II.

FEATURES OF THE INVISCID IMPINGING JET

The system of spherical polar coordinates shown in Figure 1 and the following dimensionless variables will be used:

$$r = \frac{\overline{r}}{\overline{R}}; \qquad V = \frac{\overline{V}}{\overline{U}_N} \quad (8)$$

The quantities on the right-hand side are dimensional.

In terms of these variables the velocity and stream function in the nozzle are

$$V = (1 - r^2 \sin^2 \theta) \quad (9)$$

and

$$\psi = \frac{r^2 \sin^2 \theta}{2} - \frac{r^4 \sin^4 \theta}{4} \quad (10)$$

In Figure 1 the stream surface at the nozzle wall leaves the nozzle at C, $\theta = \theta_N$ and becomes a free stream surface. The pressure across this surface is continuous, while the velocity may be discontinuous. If the fluid outside this free surface is at rest, then the pressure and the velocity (U_B) along a streamline in this surface are constant. It should be noted that U_B is not necessarily zero. Due to the presence of the impingement surface close to the nozzle exit, the pressure in the nozzle might increase leading to a pressure decrease from B to C. Since slip at a solid boundary is permitted in inviscid flow, the velocity at the wall increases.

Pressure on the deflecting surface will be a maximum at the stagnation point of the jet and will fall with increasing radial distance until it reaches that of the ambient at some distance, say, r_E. At such a distance r_E, the component of velocity normal to the deflecting surface may be neglected with respect to the horizontal component. With this assumption it is easily shown that along DE,

$$\psi = \frac{(1 + U_B{}^2) - (\sqrt{1 + U_B{}^2} - 2\, r_E h)^2}{4} \tag{11}$$

and the thickness, Δ, of the fluid on the surface at DE is given by

$$\Delta = \frac{\sqrt{1 + U_B{}^2} - U_B}{2 r_E} \tag{12}$$

Hence, while the point D on the streamline CD in Figure 1 can be determined to a good approximation, the behavior of the free surface between the nozzle exit and D is unknown and will be determined such that Equation (6), which describes the motion of the fluid in this region, is satisfied.

INVISCID SOLUTION

The velocity components defining the stream function are

$$V_r = \frac{-1}{r^2 \sin\theta} \frac{\partial\psi}{\partial\theta} \tag{13}$$

and

$$V_\theta = \frac{1}{r \sin\theta} \frac{\partial\psi}{\partial r} \tag{14}$$

$$V_\phi = 0 \tag{15}$$

Using Equation (3) the vorticity is found to be

$$\vec{\zeta} = \vec{i}_\phi \frac{E^2\psi}{r} \tag{16}$$

where E^2 is the operator

$$E^2 = \frac{\partial}{\partial r}\left(\frac{1}{\sin\theta}\frac{\partial}{\partial r}\right) + \frac{\partial}{\partial\theta}\left(\frac{1}{r^2 \sin\theta}\frac{\partial}{\partial\theta}\right) \tag{17}$$

Following Milne-Thomson (*12*), Equation (6) is satisfied by

$$E^2\psi = r^2 \sin\theta\, f(\psi) \tag{18}$$

This equation describes the inviscid flow everywhere, and if in particular, $E^2\psi$ is evaluated in the nozzle using Equation (10), one obtains

$$f(\psi) = -2 \tag{19}$$

Hence the equation governing the inviscid motion is

$$E^2\psi = -2r^2 \sin\theta \tag{20}$$

with boundary conditions:

$$\psi = 0;\ \theta = 0;\ \infty \geqq r \geqq 0 \tag{21a}$$

$$\psi = 0;\ \theta = \pi/2;\ \infty \geqq r \geqq 0 \tag{21b}$$

$$\psi = 1/4;\ 0 \leqq \theta \leqq \theta_N;\ r = 1/\sin\theta \tag{21c}$$

$$\psi = 1/4;\ \theta_N \leqq \theta \leqq \pi/2;\ r = r(\theta) \tag{21d}$$

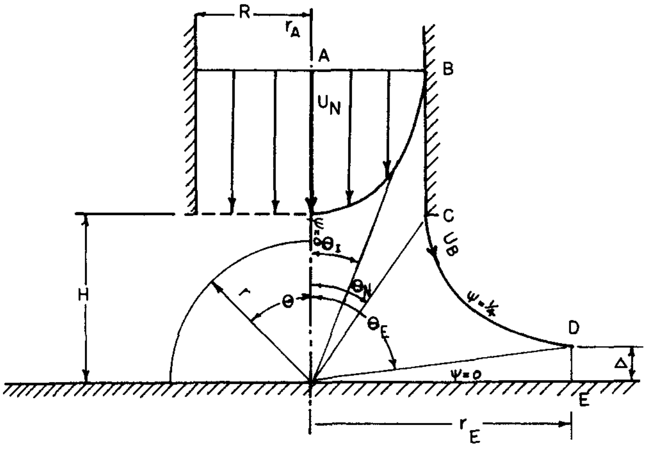

Fig. 1. Sketch of the inviscid, parabolic impinging jet (right-hand side) and uniform jet (left-hand side).

Using the method of separation of variables, and with Equation (10) as a particular solution, the solution of (20) which satisfies boundary conditions (21*a*) and (21*b*) is obtained

$$\psi = \frac{-r^4 \sin^4\theta}{4} + 2r^4 \mathcal{R}_3(\mu) + \sum_{n=1}^{\infty} A_{2n} r^{2n+1} \mathcal{R}_{2n}(\mu) \tag{22}$$

where

$$\mathcal{R}_n(\mu) = \int_{-1}^{\mu} \mathcal{P}_n(\mu)\, d\mu = C_{n-1}^{3/2}(\mu) \cdot n(n+1) \tag{23}$$

and

$$\mu = \cos\theta \tag{24}$$

The coefficients A_{2n}, $n = 1, 2 \ldots$ must be chosen such that boundary conditions (21*c*) and (21*d*) are satisfied.

DETERMINATION OF THE COEFFICIENTS A_{2n}

In view of the nature of the function within the summation and the boundary condition (21*d*) at the free surface where the boundary shape, $r = r(\theta)$, is unknown, it was necessary to determine the coefficients A_{2n} by approximate numerical methods. Restricting the solution to a finite region, the boundary conditions (21) can be rewritten for the region $ABCDE$, using Equations (10),

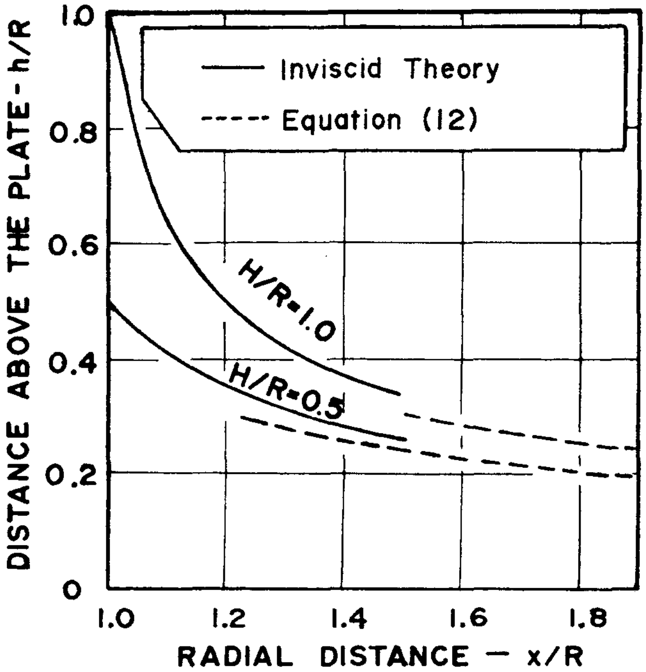

Fig. 2. Free boundary shapes from inviscid theory, $H/R = 0.5$ and 1.0.

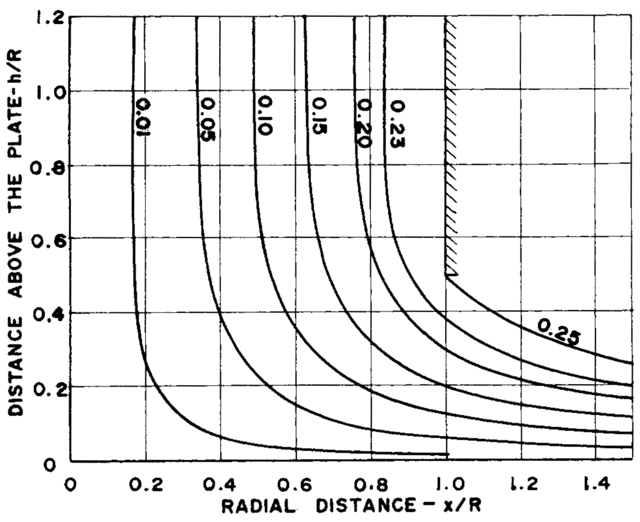

Fig. 3. Stream function, ψ, in the inviscid impinging jet, $H/R = 0.5$.

(11) and (12) giving: entry region

$$\psi = \frac{r^2 \sin^2 \theta}{2} - \frac{r^4 \sin^4 \theta}{4}; \quad 0 \leq \theta \leq \theta_I; \ r = r_A/\cos\theta \qquad (25a)$$

nozzle wall

$$\psi = 1/4; \ \theta_I \leq \theta \leq \theta_N; \ r = 1/\sin\theta \qquad (25b)$$

free boundary

$$\psi = 1/4; \ \theta_N \leq \theta \leq \theta_E; \ r = r(\theta) \qquad (25c)$$

exit region

$$\psi = (1 + U_B{}^2) - (\sqrt{1 + U_B{}^2} - 2r^2 \sin\theta \cos\theta)^2; \quad \theta_E \leq \theta \leq \pi/2; \ r = \frac{r_E}{\sin\theta} \qquad (25d)$$

The coefficients A_{2n} in Equation (22) were calculated by truncating the series solution to ten terms and obtaining a best fit to the boundary conditions (25); the sum of the squares of the residuals was minimized at a number of discrete points on the boundary (*13*). The number of points chosen was at least eight times the number of terms.

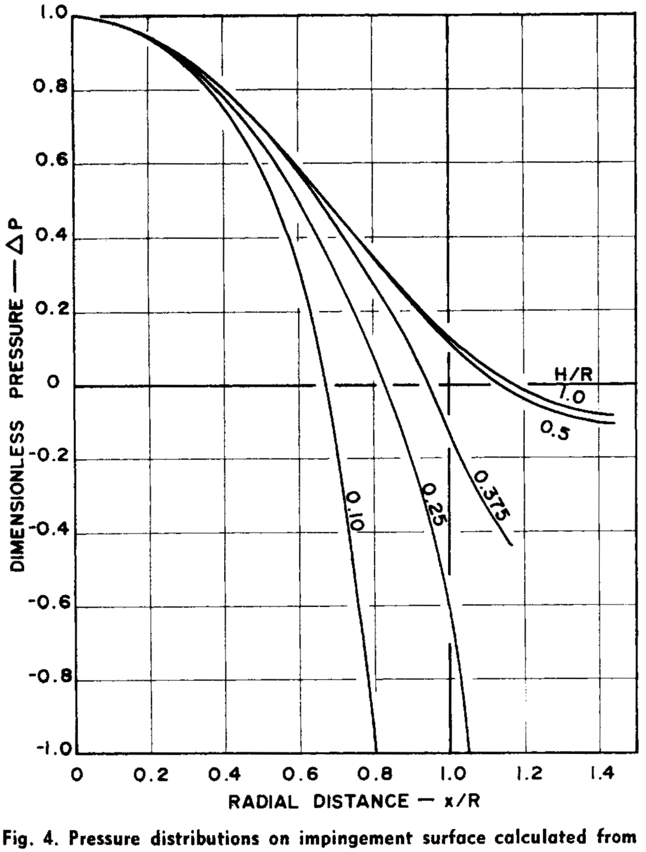

Fig. 4. Pressure distributions on impingement surface calculated from inviscid theory.

DETERMINATION OF FREE BOUNDARY SHAPE

A free boundary shape, $r = r(\theta)$, must be found such that the velocity U_B along this boundary is a constant. Such a boundary shape and velocity U_B are unique.

For $H/R = 1.0$ and 0.5 the free boundary was determined by a method of successive approximations. A free streamline shape was assumed and the constants A_{2n} calculated. From this trial solution the velocities at points along $r = r(\theta)$ were calculated. Using these velocities, the boundary shape was altered to give a second trial value (*14*). By repeating the procedure twenty or more times a boundary shape was obtained along which the variation of velocity was a minimum. Details of the numerical work which was done with the aid of a digital computer are given elsewhere (*14*).

The boundary shapes found by this method for $H/R = 0.5$ and 1.0 are shown in Figure 2. Also shown in this figure is the free boundary shape calculated from Equation (12); for $x/R > 1.5$, Figure 2 shows that Equation (12) is a fair approximation to the boundary shape.

For $H/R \leq 0.375$, the series solution converges less rapidly than for $H/R \geq 0.5$. A large number of terms is required to describe the flow for $r \approx 1$ and the numerical procedure for determining U_B and the free boundary shape was not successful; unique coefficients satisfying the constant velocity condition could therefore not be determined.

It can be deduced from Figure 2 that for this H/R range, Equation (12) will give a good approximation to the free boundary shape almost to the nozzle edge, and the undetermined length will be quite short. On this assumption, choosing a point just outside the nozzle exit, $r \approx 1.05$, the coefficients A_{2n} were calculated for various assumed values of U_B. The pressure distribution on the impingement surface was also calculated and the set of coefficients which gave a pressure distribution width in best agreement with the experimentally measured width was chosen for further calculations.

The first seven coefficients of the solution and the free boundary velocities, U_B, are given in Table 1 for $H/R = 1.0$, 0.5, 0.375, 0.25 and 0.1. For values of the radius vector, r, less than unity, the coefficients obtained by the approximate numerical technique are thought to be quite accurate. For $r > 1$, the higher order terms of solution, which are less accurately determined by the present method, are of importance and truncation errors become appreciable.

DISCUSSION OF THE INVISCID SOLUTION

Figure 3 is a plot of the inviscid solution for $H/R = 0.5$ and shows the flow behavior in the stagnation region of the nonuniform jet. The shape of the free jet boundary is given by the streamline $\psi = 0.25$. The velocity along the free portion of this streamline, which also forms the nozzle wall, is constant at 0.325. Some distance inside the nozzle the velocity at the wall is zero and there is an increase in velocity (or decrease in pressure) along this streamline from a point inside the nozzle to the ambient. Such a pressure drop will be present whenever the nozzle exit lies within the region of increased pressure near the stagnation point; flow near the axis inside the nozzle is retarded and a compensating flow acceleration is experienced by the surrounding fluid. From the theoretical plot of the axial velocity versus distance above the plate shown in Figure 6 it is apparent that only for $H/R < 1.3$ does appreciable deceleration of fluid on the axis of the nozzle occur.

From the stream function, Equation (22), and the coefficients in Table 1 it is possible to calculate the velocity and pressure distributions in the impinging jet. For $H/R \leqq 0.375$, only the form of the pressure distribution is theoretical; the width of the distribution was obtained from experiment.

The velocity along the deflecting surface is obtained from Equation (13) as

$$V = -\frac{1}{r^2}\frac{\partial\psi}{\partial\theta}\bigg|_{\theta=\pi/2} \tag{26}$$

and for $H/R = 0.5$ the first term of this expression is

$$V = 1.161\frac{x}{R} + \ldots . \tag{27}$$

This is compared to Strand's solution (*6*) for the inviscid uniform impinging jet for $H/R = 2.0$,

$$V = 0.4516\frac{x}{R} + \ldots . \tag{28}$$

For small radial distances, only the first term of Equations (27) and (28) is of significance and these expressions reduce to the classical stagnation flow (*15*) for which

$$V = \alpha x$$

where α is a constant.

Comparing the first terms of Equations (27) and (28) it is seen that the acceleration (or rate of pressure decrease) with increasing radial distance from the stagnation point for the nonuniform jet is more than twice that for the uniform jet. The flow behavior in the stagnation region of the impinging jet is, therefore, greatly influenced by the profile of the impinging jet. The first coefficients, A_2, given in Table 1 for various H/R values, show that within the accuracy of the numerical methods, flow near the stagnation point of the present jet is independent of nozzle-to-surface distance.

From the velocity distribution along the impingement surface pressure distributions on this surface can be calculated. Measuring all pressures relative to the pressure of the undisturbed parabolic flow in the nozzle, the dimensionless pressure is defined as

$$\Delta p = \frac{(p - p_N)}{\rho}\bigg/\frac{U_N^2}{2g_c} \tag{29}$$

The pressure distribution on the impingement surface is

$$\Delta p = (1 - V^2)_{\theta=\pi/2} \tag{30}$$

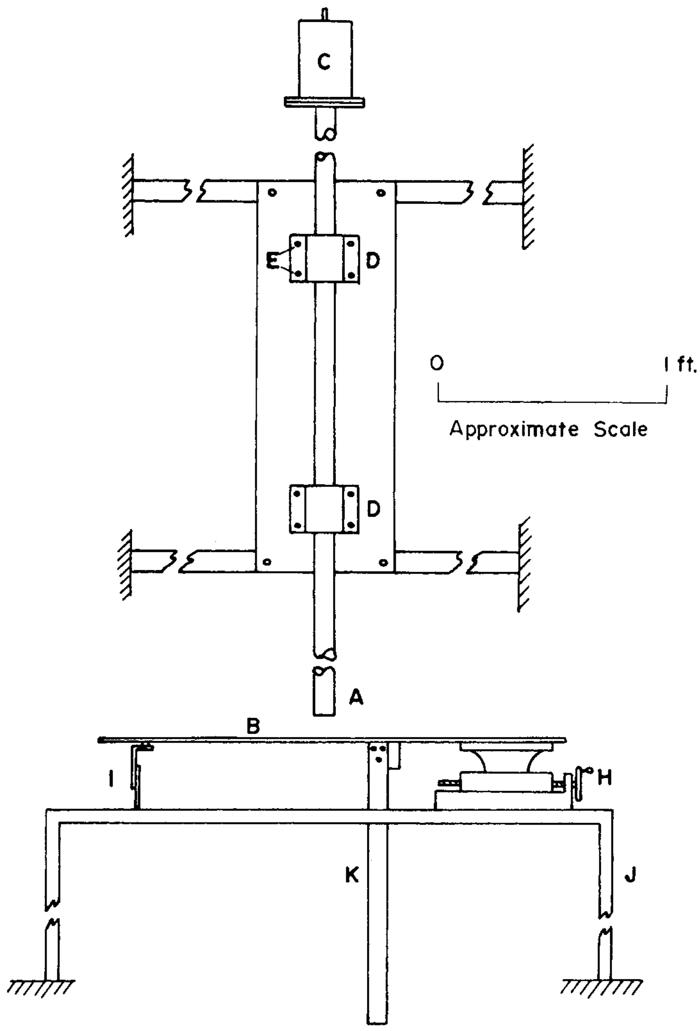

Fig. 5. Experimental equipment.

Figure 4 shows the pressure distribution on the impingement surface for various nozzle elevations. On the ordinate of this graph, 1.0 represents the stagnation point pressure, and 0.0 represents the pressure of the undisturbed flow in the nozzle.

For large nozzle elevations, $H/R >> 1$, the pressure on the impingement surface would be expected to reach a maximum at the stagnation point and then to decrease with increasing radial distance to zero as the kinetic head is recovered. For the presently considered range of nozzle heights, $0.1 \leqq H/R \leqq 1.0$, the final pressure approached for large radial distances is negative, showing that in all cases stagnation starts inside the nozzle. For $H/R = 1.0$ and 0.5 it is seen from Figure 4 that there is only a slight loss of potential head. At smaller nozzle-

Table 1.

Numerical Constants A_{2n}	Nozzle-to-surface distance — H/R				
	1.0 $U_B = 0.101$	0.5 $U_B = 0.325$	0.375 $U_B = 0.568$	0.25 $U_B = 0.926$	0.10 $U_B = 2.54$
$n = 1$	-2.323	-2.338	-2.286	-2.335	-2.433
2	-6.212×10^{-1}	-6.129×10^{-1}	-5.241×10^{-1}	-7.598	3.465×10^{-1}
3	-8.721×10^{-3}	-6.261×10^{-3}	-2.977×10^{-1}	-4.358×10^{-1}	-2.284
4	1.289×10^{-2}	1.050×10^{-2}	1.838×10^{-1}	9.367×10^{-3}	2.195
5	-8.645×10^{-4}	-7.425×10^{-4}	2.029×10^{-2}	7.003×10^{-2}	-7.373×10^{-1}
6	-2.366×10^{-4}	-1.562×10^{-4}	6.621×10^{-2}	-1.690×10^{-2}	-3.281×10^{-1}
7	3.274×10^{-5}	1.502×10^{-5}	3.247×10^{-2}	-2.078×10^{-3}	4.181×10^{-1}

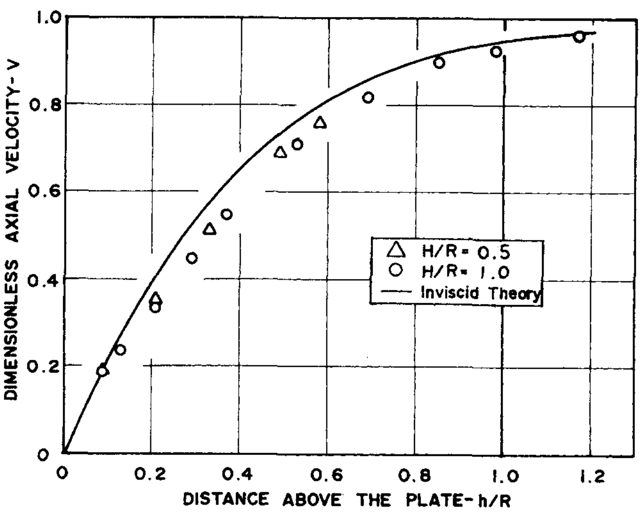

Fig. 6. Variation of axial velocity with distance above impingement surface, $H/R = 0.5$ and 1.0. Comparison with inviscid theory.

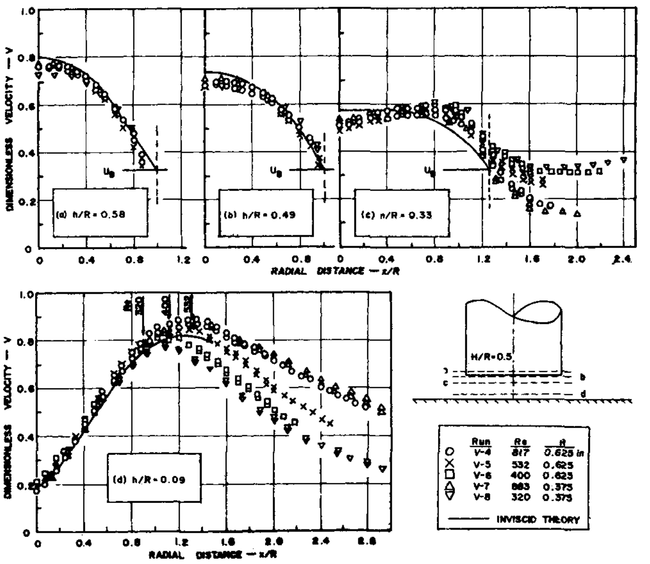

Fig. 7. Velocity profiles in the impinging jet at various distances above impingement surface, $H/R = 0.5$. Comparison with inviscid theory.

to-surface distances, however, the passage of fluid from the nozzle is restricted by the impingement surface and the pressure difference between the fluid in the nozzle and the ambient increases rapidly with decreasing nozzle height. At $H/R = 0.1$ the flow area between the nozzle and the impingement surface is only 1/5th that in the nozzle; the fluid accelerates rapidly with increasing radial distance along the surface, reaches U_N at $x/R \approx 0.66$ and attains a final veocity of $2.7U_N$ as it passes under the nozzle wall. The claculated ambient pressure relative to that in the nozzle is —6.45. The rapid loss of pressure to a value below that in the nozzle is clearly shown by the distribution in Figure 4 for $H/R \leqq 0.375$.

A pressure loss coefficient, β, which expresses the loss in fluid pressure due to constriction of the flow in terms of the kinetic energy of the fluid in the nozzle is defined as

$$\beta = \frac{p_N - p_A}{\rho} \Big/ \frac{\overline{U}^2}{g_c} \tag{31}$$

The loss coefficient approaches zero for $H/R >> 1$ and becomes infinite for $H/R \rightarrow 0$.

EXPERIMENTAL PROCEDURE

To investigate the results of the inviscid theory, two kinds of measurements were made, namely, velocity distributions in the impingement region and pressure distributions on the deflecting surface.

Equipment

The equipment is shown in Figure 5. A circular duct or nozzle A directs a jet of air towards the plane surface B. Nozzle diameters of 2.00, 1.25 and 0.75 in. were used. Sufficient length of duct was allowed to ensure full development of the parabolic laminar profile.

A calming section C containing six 200 mesh screens was provided to ensure a uniform entry of air to the nozzle section. The plane surface B, 2 × 2 ft., was fixed to an indexing head H which permitted the surface to be moved sideways. In the center of the plate was a 3/4 in. threaded hole. Plugs carrying the probes for pressure and velocity measurement could be screwed into this hole and were flush with the surface. By means of the indexing head the probe and plate could be traversed across the stagnation region and located with an accuracy of 0.001 in. The steel scale K, fixed beneath the surface, carried a vernier for accurate vertical location of the velocity probe which protruded above the surface.

Velocity Measurements

Usual methods of measuring air velocities such as the pitot tube or conventional hot wire anemometer were not sufficiently accurate for the present measurements in the range of 0.1 to 10 ft/sec. A measuring method using a hot wire anemometer and bridge circuit was developed for the accurate measurement and continuous recording of low air velocities. Briefly, the modified anemometer consists of a hot wire filament which operates at a temperature and current both of which vary with air velocity. Motion of air relative to the hot filament causes a direct current output signal from the bridge circuit. This signal was continuously monitored using a millivolt recorder. The output signal was not linear with velocity and the system had to be calibrated. This calibration was conveniently done before and after measurement with the filament at the velocity maximum of the parabolic velocity profile in the nozzle.

For the measurement of velocity profiles the anemometer was located in the flow region some distance above the surface, measured by the scale K. By means of the indexing head the probe was traversed across the axis of the impinging jet at various distances above the plate. Such a series of four traverses is shown in the inset diagram in Figure 7. Only the magnitude of the velocity vector was measured, the filament being aligned normal to the flow; flow directions were not measured. The accuracy of the dimensionless velocity measurements is estimated to be ± 3%.

Pressure Measurements

With the low velocities used, the pressures to be measured were of the order of 2×10^{-2} in. of water. A microdifferential pressure transducer was used for these measurements. The transducer had a linear output of 10 v. for 0.1 in. water.

The pressure tap was a 0.001 in. diameter hole in a 0.01 in. thick surface mounted on a plug attachment flush with the plate surface. The pressure at this tap was measured relative to the pressure in the undisturbed laminar flow in the nozzle. The nozzle pressure tap was located two nozzle diameters from the exit. The pressures at these taps were transmitted to the differential transducer using flexible tubing. As for the velocity measurements, the pressure tap was traversed across the stagnation region by means of the indexing head H. The output from the transducer was recorded using a chart recorder.

The differential pressures were corrected for the small friction loss which occurs between the nozzle pressure tap and the nozzle exit. Pressure profiles were made dimensionless by dividing through with the stagnation point pressures measured in all cases with $H/R = 1.0$; decay of the axial velocity in the jet occurs only for $H/R >> 1$ and the loss coefficient β, measured for $H/R = 1.0$ was negligible. The accuracy of these dimensionless pressure distributions is estimated to be ± 3% of the pressure maximum.

RESULTS AND DISCUSSION

Velocity Profiles

Figure 6 is a dimensionless plot of experimental velocity data taken on the axis of the jet. The axial velocity is shown plotted vs. the distance h/R above the impingement surface for $H/R = 0.5$ and 1.0. The prediction from the inviscid theory is also shown. The experimental data show no significant dependence on nozzle height for $H/R = 0.5$ and 1.0 which is in accord with the inviscid theory. While the theoretical prediction tends to lie slightly above the experimental data over most of the range, the agreement with experiment is satisfactory.

Profiles of the velocity vector in the impinging jet were measured for nozzle heights of 0.5R and 1.0R; flow directions were not determined. Figure 7 shows the data taken for $H/R = 0.5$. A dimensionless velocity V has been plotted vs. a dimensionless radial distance x/R for four distances from the deflecting surface; namely $h/R = 0.58$ (just inside the nozzle), 0.49, 0.33, and 0.09. Figure 7, therefore, gives the behavior of the velocity distribution as the jet approaches the impingement surface. These data were taken using nozzle diameters of 1.25 and 0.75 in. and Reynolds numbers in the range 320 to 883.

From the four profiles plotted, it is apparent that for a distance above the plate greater than 0.09 R and for $x/R < 1.2$, flow in the jet is well characterized using the single scales of length and velocity, R and U_N. There is no need to include the Reynolds number in either of these scales in order to achieve similarity, demonstrating the inviscid nature of the flow in the Reynolds number range tested.

The velocity profiles calculated from the theoretical solution for the inviscid, nonuniform jet are also shown in Figure 7. Allowing for the slight difference in behavior on the jet axis, noted from Figure 6, the agreement between inviscid theory and experiment is satisfactory. Not only are theoretical velocity profiles well supported by experiment, but so are the shape of, and velocity along, the free streamline. In the viscous jet, no free streamline actually exists. Viscous diffusion or vorticity from any such vortex sheet would result in the formation of a boundary layer. Where this boundary layer is thin, one might expect some correlation with inviscid theory. In Figure 7*c* the location of the theoretical boundary of the inviscid jet is indicated by the dotted line; the velocity U_B along this boundary is also shown. There is good correlation on both accounts between theory and experiment. Similar good agreement was also found with data for $H/R = 1.0$ (*14*).

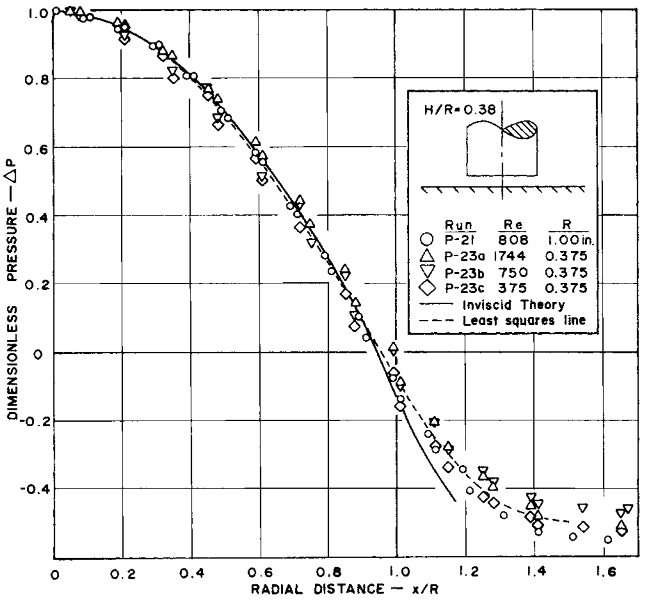

Fig. 9. Pressure distribution on impingement surface, $H/R = 0.38$. Comparison with inviscid theory.

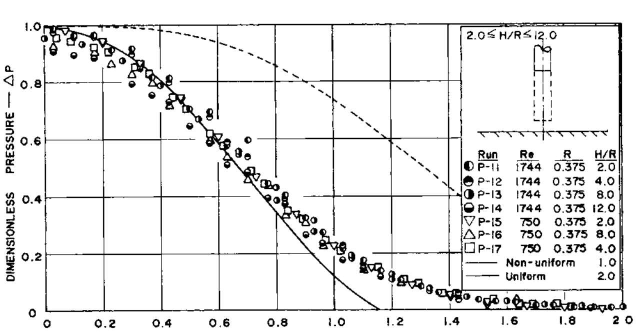

Fig. 8. Pressure distributions on impingement surface, $2 \leqq H/R \leqq 12$. Comparison with inviscid theory.

Close to the nozzle exit, Figure 7*b*, the jet was found to have a fairly distinct boundary with no detectable flow outside the jet. At a distance $h/R = 0.33$ (Figure 7), however, a well defined flow external to the jet was measured. With the growth of a viscous boundary layer along the edge of the jet, momentum is imparted to the surrounding air and pressure is reduced in the vicinity of the impinging jet, resulting in an induced external flow of air. At the lower Reynolds numbers, boundary layer development is most pronounced and the induced flow around the jet is relatively greater than at higher Reynolds numbers. In a previous investigation of the laminar wall jet (*17*), this external flow was found to be a dominant feature of the impinging jet at Reynolds numbers less than 300. The wall jet formed by the impinging jet was observed to separate from the deflecting surface and turn in towards the impinging jet with the formation of a torroidal vortex; at higher Reynolds numbers no such vortex formed. The dependence of external flow on the Reynolds number is clearly shown in Figure 7*c* by the spread of data points beyond the edge of the jet.

Closer to the impingement surface, Figure 7*d*, another viscous region of this jet is evident from the measurements. For $x/R < 0.8$ the experimental data are in good agreement with the inviscid theory. For larger radial distances, however, the velocity probe enters the laminar boundary layer on the deflecting surface and velocity data depart from the inviscid line shown. At the lowest Reynolds number, $N_{Re} = 320$, the viscous boundary layer is thickest and the velocity probe would appear to enter the boundary layer at $x/R = 0.8$, while for $N_{Re} = 532$ the inviscid nature of the jet persists out to $x/R = 1.3$. Using the boundary layer calculations given in Part II of this paper, the radial distance at which the velocity in the boundary layer decreases to 0.95 of the inviscid velocity was calculated. These calculated distances are shown by labeled arrows in Figure 7*d*; good agreement with the boundary layer theory is apparent.

The experimental work has shown the presence of two distinct boundary layer regions in the impinging jet. These boundary layers grow with distance from their respective origins and at some radial distance along the plate they will merge to form a single boundary layer. This boundary layer develops into a wall jet (*16, 17*).

Pressure Distributions

Pressure measurements at a surface have been proven

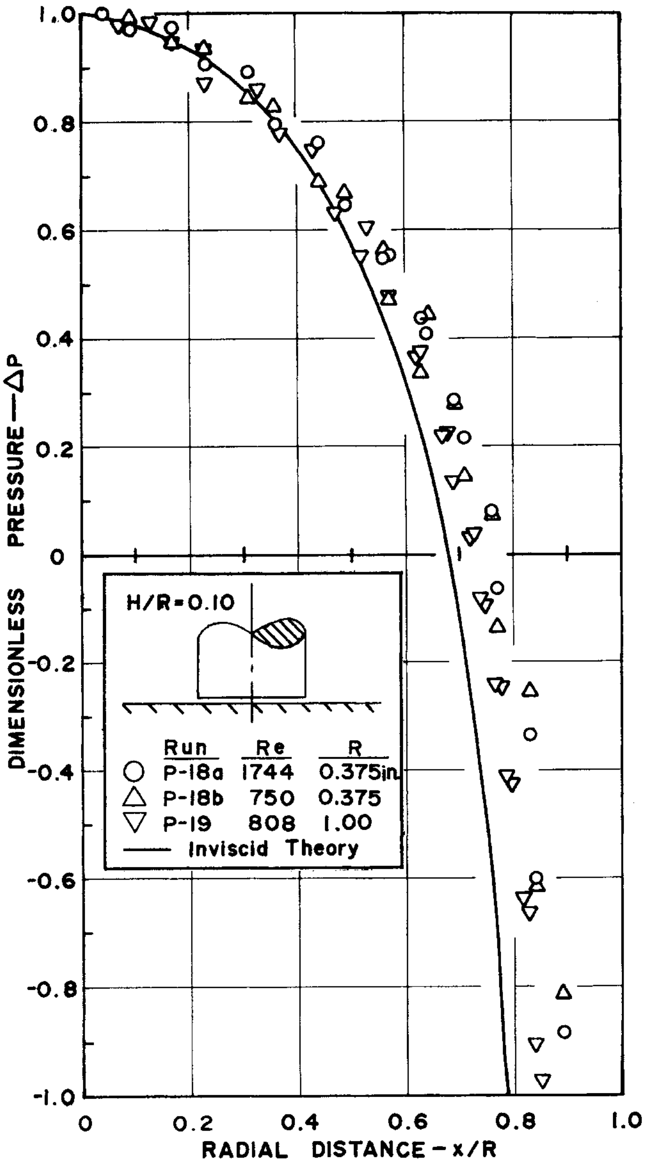

Fig. 10. Pressure distribution on impingement surface, $H/R = 0.1$. Comparison with inviscid theory.

extremely useful in fluid mechanics in that they provide information regarding the flow outside the viscous boundary layer.

Pressure distributions on the deflecting surface in the stagnation region of the impinging jet were measured in the Reynolds number and nozzle height ranges of 750 to 1,744 and $0.1R$ to $12.0R$, respectively. Nozzle diameters of 2.00, 1.25, and 0.75 in. were used. These data are shown in Figures 8 to 10. It is recalled that in these figures unity on the ordinate corresponds to stagnation point pressure and zero to the pressure of the undisturbed flow in the nozzle.

Figure 8 shows the distribution of pressure in the stagnation region for $2.0 \leq H/R \leq 12.0$. The data for $H/R = 1.0$ are indistinguishable from those plotted (*14*). Also shown is the prediction of the inviscid theory for $H/R = 1.0$. The experimental data have generally a broader distribution than the theoretical calculations. From Figure 8, the pressure at the stagnation point of the jet decreases only slightly with increasing nozzle height, and the width of the distribution is little affected. This would indicate that there is very little spreading of the jet for $H/R \leq 12.0$. Some degree of transition to a free jet profile must occur, and at elevations much greater than $12R$ decay of the center line velocity and, therefore, the stagnation point pressure would be expected.

Also shown dotted in Figure 8 is the pressure distribution calculated from Strand's solution for a uniform jet. The uniform jet pressure distribution is considerably wider than that for the nonuniform jet, most of the kinetic energy in the nonuniform jet being concentrated close to the jet axis.

Figure 9 gives the data for $H/R = 0.38$ along with the prediction of the inviscid theory. Unlike the distribution in Figure 8, the pressures for $x/R > 0.95$ become negative with respect to that in the undisturbed flow in the nozzle. The inviscid theory for $H/R = 0.38$ gives a velocity on the free stream boundary of 0.568, which from Equation (31) shows that there is a loss of potential head due to the proximity of the plate to the nozzle exit. This predicted decrease in pressure, below that in the nozzle, is clearly shown by the data in Figure 9.

With the nozzle still closer to the plate, the resistance to flow is even greater. The data for $H/R = 0.1$ are shown in Figure 10. The pressure on the plate decreases rapidly from a maximum on the axis and passes steeply through zero at $x/R \approx 0.63$. The measured dimensionless ambient pressure in this case was -15 compared with -6.45 predicted from inviscid theory. At low clearances between nozzle and surface viscous friction cannot be neglected. The displacement thicknesses of the boundary layer at the nozzle edge and on the impingement surface would reduce the effective nozzle-to-surface distance; this would increase the pressure drop further.

In Figure 11, the experimental values of the loss coefficient are compared with those obtained from the inviscid theory. At values of H/R of the order of 0.1, departure of theory from experiment is largest, due to viscosity effects. At values of $H/R > 0.2$ the agreement between theory and experiment is satisfactory.

SUMMARY AND CONCLUSIONS

A theoretical solution for the impingement flow of a jet with a parabolic velocity distribution has been obtained; viscous generation and diffusion or vorticity in the jet were neglected and the resulting inviscid equations solved. The results of the theoretical work are compared with experimental velocity and pressure distributions measured in an impinging jet of air originating with

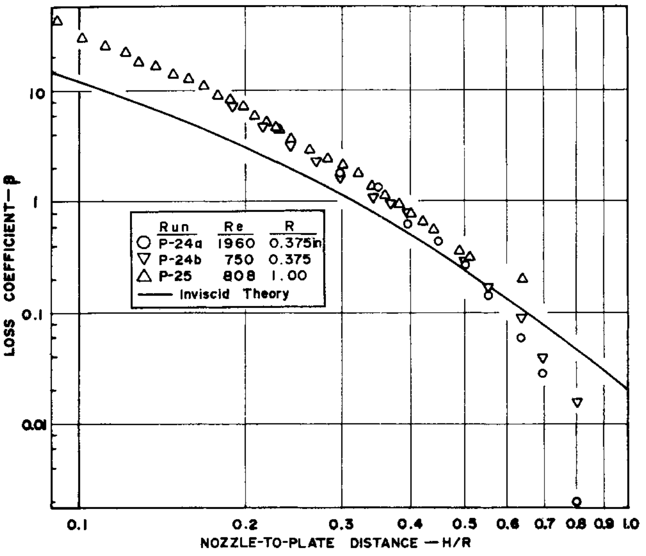

Fig. 11. Pressure loss coefficient, β. Comparison with inviscid theory.

Poiseuille flow; good agreement between experiment and inviscid theory is reported.

Velocity distributions in the impinging jet were measured for nozzle-to-surface distances of 0.5 and 1.0R. Except for the boundary layer regions close to the impingement surface and at the edge of the jet, the velocity data are independent of Reynolds number, demonstrating the inviscid nature of the jet.

Pressure distributions on the impingement surface were measured for nozzle heights in the range 0.1 to 12R. The data for $H/R \geqq 1.0$ show no significant dependence on either Reynolds number or nozzle height. For $H/R < 1.0$ the effect of flow constriction between the nozzle and the surface becomes apparent as the nozzle wall is approached. Close to the stagnation point, $x/R << 1$, flow is, however, not influenced by nozzle height in the range tested. The flow constriction results in a pressure loss which increases rapidly with decreasing H/R.

ACKNOWLEDGMENT

Financial assistance from the National Research Council of Canada is gratefully acknowledged.

NOTATION

A_{2n} = constant coefficients in inviscid solution
$C_n^{3/2}(\mu)$ = Gegenbauer polynomial
D = nozzle diameter, ft.
g_c = gravitational conversion factor, lb.$_m$-ft./lb.$_f$-sec.^{2}
h = normal distance from surface, ft.
H = nozzle-to-surface distance, ft.
$\vec{i}_\phi$ = unit vector
p = pressure, lb.$_f$/sq. ft.
p_A = ambient pressure, lb.$_f$/sq. ft.
p_N = pressure inside nozzle, lb.$_f$/sq. ft.
$\mathcal{P}_n(\mu)$ = Legendre function of the first kind
r = spherical polar coordinate
R = nozzle radius, ft.
$\mathcal{R}_n(\mu)$ = function defined by Equation (23)
U_N = velocity maximum in nozzle, ft./sec.
U_B = velocity along free streamline
$\overline{U}$ = average velocity in nozzle, ft./sec.
$\vec{V}$ = velocity vector, ft./sec.
V = velocity
v_r = velocity component in r direction
v_θ = velocity component in θ direction
v_ϕ = velocity component in ϕ direction
x = radial distance along surface, ft.

Greek Letters

β = pressure loss coefficient, Equation (31)
δ = boundary layer thickness, ft.
Δ = value of h on free boundary
Δp = dimensionless pressure
$\vec{\zeta}$ = vorticity vector
θ = spherical polar coordinate
μ = $\cos\theta$
ν = kinematic viscosity, sq. ft./sec.
ρ = density, lb./cu. ft.
ϕ = spherical polar coordinate
ψ = stream function

Dimensionless groups

N_{Re} = Reynolds number = $\overline{U}D/\nu$

LITERATURE CITED

1. Brady, W. G., and G. Ludwig, *Inst. Aerospace Sci., Paper No. 63-29* (1963).
2. Leclerc, A., M.Sc. Thesis, State Univ. Iowa (1948).
3. Ranz, W. E., and P. F. Dickson, Univer. Minnesota, private communication (1962).
4. Schach, W., *Ing. Archiv.*, **6**, 51 (1935).
5. Shen, Y. C., *Inst. Aerospace Sci., Paper No. 62-144* (1962).
6. Strand, T., *Am. Inst. Aeron. Astronaut paper No. 64, 424* (1964).
7. Gardon, R., and J. Cahit Akfirat, *Intern. J. Heat Mass Transfer*, **8**, 1261 (1965).
8. Sutera, S.P., P. F. Maeder, and J. Kestin, *J. Fluid Mech.*, **16**, 497 (1963).
9. Rao, V. V., and Olev Trass, *Can. J. Chem. Eng.*, **42**, 95 (1964).
10. Dawson, D. A., and O. Trass, *ibid.*, **44**, 121 (1966).
11. Schrader, H., *VDI-Forsh. -Heft.*, 484, Düsseldorf (1961).
12. Milne-Thomson, L. M., "Theoretical Hydrodynamics," 3rd Ed., p. 527, Macmillan and Co., London, (1956).
13. Crandel, S. H., "Engineering Analysis: A Survey of Numerical Procedures," McGraw-Hill, New York (1956).
14. Scholtz, M. T., Ph.D. dissertation, Univ. Toronto, (1965).
15. Schlichting, H., "Boundary Layer Theory," 4th Ed., McGraw-Hill, New York (1960).
16. Glauert, M. B., *J. Fluid Mech.*, **1**, 625 (1956).
17. Scholtz, M. T. and O. Trass, *AIChE J.*, **9**, 548 (1964).

Part II. Boundary Layer Flow-Mass Transfer

Exact solutions of the boundary layer equations were used to calculate the local mass transfer coefficients for an impinging jet with a parabolic velocity distribution. Boundary conditions were obtained from an inviscid flow solution and also from experimental pressure distributions. Experimental data for the air/naphthalene system were in good agreement with theoretical results. Mass transfer from the impingement surface was independent of nozzle height in the range 0.5 to 12 nozzle radii. For lower nozzle heights the effect of the constriction of flow between the nozzle and the surface led to increased transfer rates near the nozzle wall; data followed the predicted behavior.

Part I of this paper deals with that region of the flow of an impinging nonuniform jet which can be considered to be external to viscous boundary layers. In this part of the paper the viscous boundary layer on the impingement surface, characterized by the impingement flow of Part I, is examined.

The viscous boundary layer which develops on the impingement surface is initially laminar, although transition to a turbulent boundary layer may occur some distance from the stagnation point. Brady and Ludwig (*1*) made experimental velocity measurements in the boundary layer of the turbulent uniform impinging jet and these were compared with velocity profiles calculated using experimental pressure distribution data; the critical radial distance from the stagnation point for neutral boundary layer stability was also calculated. From their measurements it was concluded that significant penetration of turbulence into the laminar boundary layer does occur for radial dis-